ORIGINAL PAPER

Customization of the CEFM for predicting stress corrosion cracking in lightly sensitized Al–Mg alloys in marine applications

Sang-Kwon Lee · Pengcheng Lv · Digby D. Macdonald

Abstract The Coupled Environment Fracture Model (CEFM) has been modified and calibrated to predict crack growth rate (CGR) in aluminum marine alloys. The customized CEFM provided quantitative predictions of the effects of O_2, electrochemical potential, stress intensity factor, and conductivity on CGR in lightly sensitized AA5083-H321 in 3.5 wt.% NaCl solution, as well as explaining the development of a semi-elliptical surface cracks. The importance of the properties of the external environment, such as conductivity, oxidant/reductant concentration, and the kinetics of the cathodic reactions on the surfaces external to the crack has been confirmed. Crack growth is attributed to a sequence of microfracture events at the crack front, the frequency of which is determined by the mechanical conditions that exist at the crack tip, as governed by the stress intensity while the microfracture dimension is determined by hydrogen-induced fracture, with the CGR being the product of these two quantities. The success in explaining the intergranular stress corrosion cracking (IGSCC) of aluminum alloys, argues that the basic concept of the CEFM, that the internal and external environments are strongly coupled, is sound and that the CEFM, which was originally developed to describe IGSCC in sensitized stainless steels is equally applicable for describing IGSCC in lightly sensitized aluminum alloys.

Keywords Stress corrosion cracking · Al–Mg alloys · The coupled environment fracture model · Semi-elliptical crack shape

S.-K. Lee
Center for Electrochemical Science and Technology, Department of Materials Science and Engineering, Pennsylvania State University, University Park, PA 16802, USA

P. Lv
AlphaSense, Inc., Wilmington, DE 19808, USA

D. D. Macdonald
Department of Materials Science and Engineering, University of California at Berkeley, Berkeley, CA 94720, USA

D. D. Macdonald (✉)
Center of Research Excellence in Corrosion Research Institute, King Fahd University of Petroleum and Minerals, Dhahran 31261, Saudi Arabia
e-mail: macdonald@berkeley.edu

Introduction

The need to reduce fuel consumption in marine applications, including naval vessels, has generated strong interest in weight reduction through the use of strong, lightweight materials. Al–Mg alloys (5xxx series) are the materials of choice for components that require moderate strength, good formability, good weldability, and excellent atmospheric corrosion resistance. However, Al–Mg alloys containing more than 3 wt.% Mg are susceptible to Intergranular Stress Corrosion Cracking (IGSCC) when exposed to elevated temperatures (≥50 °C) for a sufficient length of time in corrosive environments [1]. These susceptibilities result from the precipitation of highly anodic β-phase (Mg_2Al_3) that has been observed to be continuous or discontinuous at triple points and along grain boundaries [2, 3], resulting in "sensitization." Although the exact mechanism of sensitization is still controversial, the practical result is that during exposure to corrosive environments, galvanic coupling occurs between these grain-boundary precipitates and the grain interiors, which can lead to severe intergranular attack and further causes IGSCC

failures under a sufficient high tensile stress. This fact may ultimately impose limits on the use of these alloys in naval systems.

Considerable research has been reported on investigating the IGSCC behavior of sensitized Al–Mg alloys [3–16]. Several investigators have reported on the influence of metallurgical/microstructural factors on the SCC susceptibility of the alloys. Thus, Davenport et al. [14] reported that the SCC susceptibility of the sensitized AA 5182 depended strongly upon the sensitization time and temperature. Searles et al. [10] found that the ductility of AA5083 that had been sensitized at 150 °C for 333 h relied strongly on the degree of sensitization (DoS). In addition to β-phase precipitation, segregation of elemental magnesium to grain boundaries during elevated temperature exposure of Al–Mg alloys has also been investigated [5, 6, 8, 9], but there are conflicting reports about its effect on SCC. For instance, Windisch et al. [8] reported that Mg enrichment promoted corrosion of aluminum in 3.5 wt.% salt solution at pH of 10. However, Baer et al. [9] stated that, although alloys with magnesium segregation and β-phase precipitates on the grain boundaries were more susceptible to SCC, the segregated Mg had little effect on the actual cracking process. This observation was supported by a later work of Jones et al. [3] who studied the role of Mg in the SCC of the AA5083-H321 alloy. They found that elemental magnesium that had segregated to grain boundaries did not contribute to SCC of the alloy. Likewise, most studies have focused on the influence of microstructure along the grain boundaries on the SCC behavior, and this microstructural characteristic is one of the important factors in the SCC behavior of Al–Mg alloys.

However, crack advance in SCC is the result of the combined and synergistic interaction of a susceptible material, mechanical stress, and a corrosive environment. There are only a few studies on the effect of environmental variables, such as electrochemical potential (ECP) and solution conductivity. As reported by Jones et.al. [3], the crack growth rate (CGR) of AA5083 that had been sensitized for 1 h at 175 °C increased with increasing potential at potentials anodic to the open circuit value with no increase in CGR at potentials cathodic to the open circuit potential (OCP), even in materials with low precipitation of the β-phase on the grain boundaries. In addition, the effect of hydrogen on the IGSCC of pure Al–5Mg alloy with low precipitation of the β-phase on the grain boundaries in deaerated AlCl$_3$ solution was reported by Tanguy et al. [11]. They argued that anodic dissolution is necessary for the formation of a local effective medium in the crack but that it is not directly responsible for crack advance. Instead, they argue that crack advance results from failure of the interfaces of the grain boundaries and that can be attributed to an interaction between hydrogen and plasticity at the grain boundaries. We argue for a similar mechanism in this paper, but we posit that dissolution is an essential component of the mechanism, because it results in the acidification of the crack tip environment and in the displacement of the crack tip potential to a sufficiently negative value, such that injection of hydrogen occurs into the alloy matrix ahead of the crack tip.

Along with experimental studies, theoretical modeling of SCC in a variety of metals and alloys has also been vigorously pursued in order to explore the fracture mechanisms and to estimate the impact of the chemical and electrochemical conditions (e.g., potential) on CGR in a variety of metals and alloys in aqueous solutions [17–30]. Ideally, such models should be "deterministic," with the predicted phenomena or dependent variable (CGR, crack tip and mouth potentials, and crack enclave chemistry) being explicitly constrained by the natural laws (e.g., the conservation of charge and Faraday's law of mass-charge equivalency). From a scientific philosophical viewpoint, such an approach requires the formulation of a "general" model; i.e., a model that is capable of accounting for all of the empirical knowledge of the system. Thus, Turnbull [26] modeled the crack chemistry in a sensitized stainless steel in boiling water reactor (BWR) coolant environments where the medium is basically high-temperature (288 °C), pure water of low conductivity, and found that the crack tip potential is not independent of the external potential, in agreement with measurement. This same finding had been previously predicted by the Coupled Environment Fracture Model (CEFM) [22–25], as discussed below, but which also showed that the CGR should be a function of the kinetics of the cathodic reactions on the surfaces external to the crack [23], again in agreement with empirical knowledge. Ford [18–20] et al. developed a model for environmental cracking, but the model fails to invoke charge conservation explicitly and, hence, is essentially empirical in nature. Accordingly, the model does not meet the minimal conditions required for determinism, nor does it specifically account for the influence of the external environment on crack growth in an analytical manner.

Macdonald and coworkers [22–25] developed the CEFM for estimating CGR in type 304 stainless steel under BWR coolant conditions (water at 288 °C). One of the important features of this model is that it describes analytically the positive current that flows from the crack through the solution to the external surface and the electron ("coupling") current that flows through the metal from the crack tip to the external surface, as dictated by the differential aeration hypothesis (DAH; Fig. 1). This prediction is in agreement with observation made by Manahan et al. [31]. These two currents annihilate at the external interface via a "charge transfer" reaction, which is most commonly the reduction of oxygen and/or
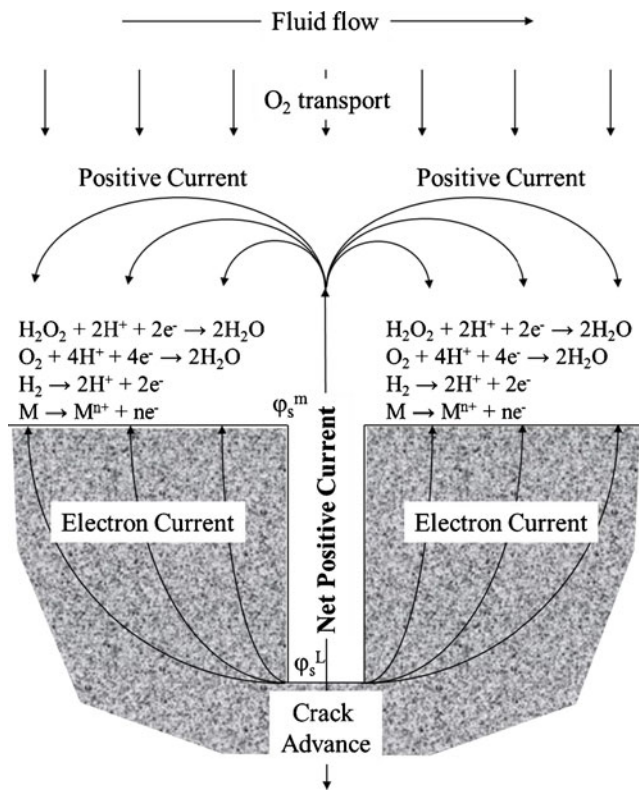
Fig. 1 Illustration of the DAH for localized corrosion [22]. φ_s^m and φ_s^L represent the electrostatic potentials in the solution at the crack mouth and at the crack tip, respectively

hydrogen evolution. The CEFM also invokes the natural law of charge conservation, in order to specify the crack mouth potential, and the electro-neutrality principle to estimate the crack tip potential, thereby rendering the model deterministic. The model itself is based upon the DAH that is considered to be the physical basis of localized corrosion phenomena, such as pitting corrosion, SCC, and crevice corrosion, and which has stood the test of time for about 80 years. The important aspect that differentiates the CEFM for SCC from others is that the positive current must be consumed through the reduction of cathodic depolarizers, such oxygen and/or hydrogen ion or water, on the external surface, which represents strong electrochemical coupling between the crack internal and external environments. In the present work, we have modified and customized the CEFM in order to describe IGSCC in aluminum alloys and to predict CGR in marine applications. It should be noted that our work is focused on aluminum alloys having low DoS since calibrating CGR data are not available for a wide range of sensitization conditions. Calibration involves optimization of the CEFM on measured CGR data, in order to extract values for poorly known model parameters and the insertion of appropriate values for aluminum for those parameters that are more accurately known.

Theory and calculation

Basis of the coupled-environment fracture model

The physico-electrochemical basis of the CEFM is the DAH, as shown in Fig. 1, and the governing system equation in the CEFM is a statement of charge conservation that renders the model deterministic. The conservation of charge can be expressed as follows:

$$i_{crack}A_{crack \cdot mouth} + \int_S i_C^N ds = 0 \qquad (1)$$

where i_C^N is the net (cathodic) current density due to the charge transfer reactions on the external surface, and ds is an increment in the external surface area. Likewise, i_{crack} is the net positive current density flowing from the crack mouth; i.e., the difference between the positive current due to anodic reactions and the negative current due to reduction processes that occur within the crack, with the anodic processes dominating. The subscript S on the integral indicates that the integration is to be performed over the entire external surface and $A_{crack\ mouth}$ is the area of the crack mouth.

The CEFM performs its calculations in two steps. In the first step, it calculates the ECP on the external surface; in the second step, the CGR is estimated. The electrostatic potential relatively far from the crack is assumed to be unchanged by the presence of the crack and, hence, is equal to the (negative of the) free corrosion potential (the ECP). As all "electrostatic" potentials shown in Fig. 1 are those within the solution, they are all defined with respect to a common reference electrode or with respect to the metal, which is regarded as being an equipotential volume. Note that the choice of reference electrode is strictly immaterial, as we are interested only in potential differences. The ECP is calculated by using the Mixed Potential Model (MPM) [32] in the CEFM for specified concentrations of O_2, H_2, and H_2O_2 (or any other redox couple) in the solution and by taking into account the kinetics of the reduction of oxygen, hydrogen peroxide, and H^+ (or water), the kinetics of the electrodissolution of the alloy, and the assumed hydrodynamic conditions. The calculated mixed potential (the ECP) is referred to the Standard Hydrogen Scale (SHE). The calculated ECP is constrained by the conservation of charge at the interface, by requiring that the sum of partial currents on the surface is equal to zero.

In the CEFM, the CGR calculation relies on splitting the total environment of the system into the crack-internal and crack-external environments (Fig. 1). The crack mouth acts as the boundary between sub-environments. An ECP at the crack mouth is firstly calculated by solving Laplace's equation for the external environment or it is assumed and the internal current generated by metal electrodissolution at the crack tip

and the external current due to reduction of the cathodic depolarizer on the external surfaces, both of which depend upon the crack mouth potential, are then calculated iteratively by iterating on that potential until the two are equal. This corresponds to the condition expressed by Eq. (1). For calculating the external current, a 40-term Fourier series solution to Laplace's equation is assumed, with the coefficients being selected to conform with the exponential-like decay of the potential with distance from the crack mouth. For calculating the internal crack current, an ECP is assumed at the crack tip. This potential is changed iteratively until electro-neutrality is satisfied at the crack tip. Thus, the calculation essentially involves the crack tip iterative loop embedded in the crack mouth iterative loop, until convergence on the current and on the crack tip potential are achieved. The electrochemical properties achieved at the crack tip depend upon the mechanical state (stress intensity) imposed on the system, upon the electrodissolution reaction at the crack tip, and upon the properties of the external environment through the kinetics of the cathodic reactions occurring on the external surfaces. Knowledge of both the crack tip and crack mouth potentials then allows calculation of the CGR and specification of other properties, such as the crack tip pH, $[Cl^-]$, $[Na^+]$, etc. For a more detailed description of the basic CEFM, the reader is referred to Refs. [22–25].

At this point, it is important to note that while the CEFM is based upon the slip-dissolution-repassivation (SDR) mechanism, it differs from that proposed by Scully [33] and by Ford and Andresen [18–20] in one important respect; the microfracture dimension is not determined by slip, which, according to the SDR mechanism, should be some small multiple of the Burgers vector for the slip system or nanometers in dimension. Experiment shows that this postulate is untenable [31, 34–36]. Instead, in the case of IGSCC in sensitized type 304 SS in high-temperature water [31] and in thiosulfate solution [34, 35] at ambient temperature, and for IGSCC in AISI 4340 high-strength steel in caustic solutions [36] at 70 °C, the fracture dimension is much larger (2–3, >100, and 40–50 μm, respectively) than can be accounted for by slip and it was concluded, in all three cases, that the microfracture dimension was determined by the spacing of precipitates on the grain boundaries and/or by hydrogen-induced cracking, or by both. In the latter case, the hydrogen is envisioned to be produced by hydrogen evolution at the crack tip, resulting from the low pH and very negative potential, both of which resulting from differential aeration [22], with the hydrogen evolution current being a small fraction of the coupling current, as indicated by the lack of hydrogen gas flooding of the crack. Thus, hydrogen-induced cracking (HIC) is an integral part of the CEFM that is presented in this paper and elsewhere. It is our postulate that the same basic mechanism is responsible for IGSCC in lightly sensitized aluminum alloys.

Customization of the CEFM to aluminum alloys

The key factor in the crack advance in the stress corrosion cracking of an Al–Mg alloy is the anodic dissolution of grain-boundary β-phase and the associated hydrogen ion reduction that accompanies this dissolution reaction [3, 7, 10, 12–14]. However, when the β-phase exists as discrete particles along the grain boundary, the crack growth between the particles is thought to result from uptake of hydrogen and hydrogen-induced crack growth [3], as noted above. The grain-boundary precipitates may also serve to define the dimension of a microfracture event, with the crack propagating intermittently from one precipitate to the next. Recently, Gao and Quesnel [16] provided evidence supporting the potential contribution of hydrogen embrittlement in the failure of grain-boundary ligaments between β-phase precipitates at the grain boundary in less severely sensitized conditions. In this sense, the cracking of aluminum alloys is mechanistically a little different from that proposed for IGSCC in type 304 SS [18–26, 30, 31, 33–35] and high-strength AISI 4340 low alloy steel [36], but, of course, all differs in the finer details.

As emphasized above, crack advance in the current version of the CEFM is postulated to occur via HIC, as shown by the stainless steel work [31, 34, 35]. Anodic dissolution, as embodied in the slip-dissolution model of Scully [33] and Ford and Andresen [18–20], and HIC are, nevertheless, closely related, as anodic dissolution, which is the result of brittle microfracture exposing bare metal at the crack tip, supplies the positive coupling current that produces the conditions within the crack (low pH and potential) that allows for hydrogen evolution and hence the injection of H into the matrix ahead of the crack, resulting in HIC. Thus, anodic dissolution and HIC are tightly coupled and both are believed to occur simultaneously in many alloys, including aluminum alloys. We expand on this issue in more detail in the "Discussion."

For customizing the CEFM to aluminum alloys, initially the environmental, electrochemical, and mechanical parameters used in the CEFM for stainless steels were substituted with values for AA 5083-H321 in aerated 3.5 wt.% NaCl solutions [37–45]. The parameter values adopted in this work are summarized in Table 1. In some cases, the parameter values had to be estimated for AA5083-H321 within a reasonable range from values for other materials, for example, pure aluminum since the available electrochemical kinetic data for aluminum alloys are insufficient to do this directly for AA 5083-H321.

Customization involves optimization of the CEFM on measured CGR data taken from the literature [3], as a function of the independent variables of interest. This procedure was begun by fitting the lumped crack-tip parameters in the CEFM to a single experimental CGR datum,

Table 1 Values for parameters in the CEFM for AA5083-H321

Parameter	Value	Comment/source
Tafel slope for HER	0.117 V	[37]
i_o for HER	1.5×10^{-9} A/cm^2	[37]
Tafel slope for ORR	0.56 V	[40]
i_o for ORR	3.04×10^{-10} A/cm^2	[41]
Passive current density at steady state	1.69×10^{-6} A/cm^2	Assumed to be 1 order in magnitude lower than the value obtained from a potentiodynamic scan [41]
E^o, standard electrochemical potential for aluminum dissolution reaction	-1.66 V$_{SHE}$	[42]
ε, strain at fracture of the passive film	1.3×10^{-3}	[38]
E, Young's modulus	70.3 GPa	[45]
σ_c, critical local stress	$1 \times 10^{-2} E$	[39]
G, shear modulus	26.4 GPa	[43]
Grain-boundary self-diffusion coefficient	8.75×10^{-5} m^2/s	[43]
Activation energy for diffusion	84 KJ/mol	[43]
Grain-boundary diffusion width	0.5726 nm	[43]
Atomic volume	6.6167×10^{-29} m^3	Calculated
Yield strength	227.53 MPa	[45]
Atomic weight	26.98 g/mol	Property tables
Metal density	2.7 g/cm^3	Property tables

HER hydrogen evolution reaction, *ORR* oxygen reduction reaction

corresponding to an ECP value of -0.51 V$_{SHE}$, which is the OCP of AA5083-H321 in aerated 3.5 wt.% NaCl solution, and the solution conductivity at 25 °C (0.078 S/cm, which is a much higher conductivity than exhibited by pure water BWR environments). High solution conductivity enhances the throwing power of the current from the crack mouth and gives the external surface a great capacity to consume electrons being released by metal dissolution at the crack tip. Therefore, environmental effects of the external surface might be more significant than those in BWR environments. After the above-fitting procedure was accomplished, a sensitivity analysis was performed on the model predictions, with one parameter being varied at a time, within a reasonable range, and for which some experimental information was available.

Results and discussion

Jones et al. [3] have reported CGR measurements for AA5083-H321 aged for 1 h at 175 °C in 3.5 wt.% NaCl solution. The sensitization at this condition corresponds to a DoS of 6.3 mg/cm^2 from the Nitric Acid Mass Loss Test (NAMLT) [46], as determined in our laboratory with the same material sensitized under the same conditions. The NAMLT is currently the accepted method for quantifying

the DoS of 5xxx marine aluminum alloys. The DoS value of 6.3 mg/cm^2 indicates that the AA5083-H321 in the study of Jones et al. [3] is lightly sensitized. They measured the CGR as a function of applied potential with compact tension specimens and showed a clear dependence of the CGR on the applied potential. Figure 2 shows the experimental CGR data for AA5083-H321 extracted from the literature [3] and the predicted CGR vs. ECP, as a function of solution conductivity. The majority of the experimental data fall within the band defined by the calculated CGR with respect to ECP as solution conductivity was varied over the selected range. The ECP was calculated using the CEFM for the concentration of O$_2$ in the solution being 6.42 ppm (2.0×10^{-4} m) [47], for the kinetics of electrodissolution of the aluminum substrate, and for the assumed hydrodynamic conditions using the MPM. As expected from electrochemical theory, as embodied in the CEFM, the CGR exhibits a strong correlation with ECP within the range -0.6 V$_{SHE}$ < ECP < -0.3 V$_{SHE}$, over which the CGR changed by ~2 orders of magnitude. At ECP values more negative than approx. -0.6 V$_{SHE}$, the CGR is dominated by the mechanical creep which is described by the Wilkinson and Vitek model [48], and the rate becomes insensitive to the ECP. Thus, for the particular conditions assumed in Fig. 2, the critical potential for IGSCC in AA5083-H321 (E_{IGSCC}) is estimated to be -0.6 V$_{SHE}$.
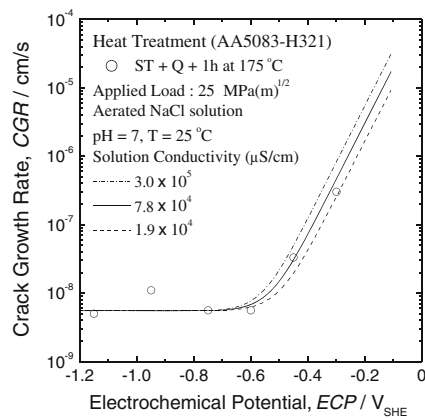
Fig. 2 Plots of the experimental data [3] and calculated CGR vs. ECP for AA5083-H321 in NaCl solutions as a function of solution conductivity at pH=7 and at 25 °C. Other parameter values as in Table 2

Effects of [O$_2$], [H$_2$O$_2$], and [H$_2$]

Predicted plots of ECP and CGR vs. [O$_2$] and [H$_2$O$_2$] for AA5083-H321 in 3.5 wt.% NaCl solution at 25 °C are shown in Fig. 3a. The CEFM predicts that the CGR increases strongly with increasing oxidizer (O$_2$ and H$_2$O$_2$) concentration and increasing ECP above certain oxidizer concentrations. At O$_2$ concentrations lower than about 3 ppm (9.3×10^{-5} m), the CGR is predicted to drop to about 5.5×10^{-9} cm/s and becomes independent of ECP as the reduction of oxygen apparently is not instrumental in consuming the electrons being produced at the crack tip, although part of the current may be consumed by hydrogen evolution, which occurs at a much more negative potential than does oxygen reduction. It is also evident that, for 3 ppm of O$_2$, the ECP falls below (becomes more negative than) the critical potential, E_{IGSCC}. Below the critical potential, the contribution of creep to the CGR is larger than that of the environmentally induced component and hence the overall CGR is controlled by mechanical effects (i.e., creep). Aluminum alloys are sufficiently ductile at ambient temperature for creep to occur, as shown in several papers [49–51]. However, when sufficient O$_2$ is present in the solution, the CGR is controlled by environmental effects, as ECP> E_{IGSCC}. From the comparison between both oxidizers, it is recognized that, on an equivalent concentration basis above 20 ppm, H$_2$O$_2$ is a stronger oxidizing agent than is O$_2$ and hence has a higher impact on CGR than does oxygen. This corresponds to the fact that H$_2$O$_2$ is more effective in displacing the ECP in the positive direction, which can be attributed largely to the more positive standard potential for the H$_2$O$_2$–H$_2$O couple than for the O$_2$–H$_2$O couple.

The importance of water chemistry parameters, such as conductivity and oxidant/reductant concentration, in SCC of type 304 SS in BWR environment has been confirmed experimentally and theoretically in many
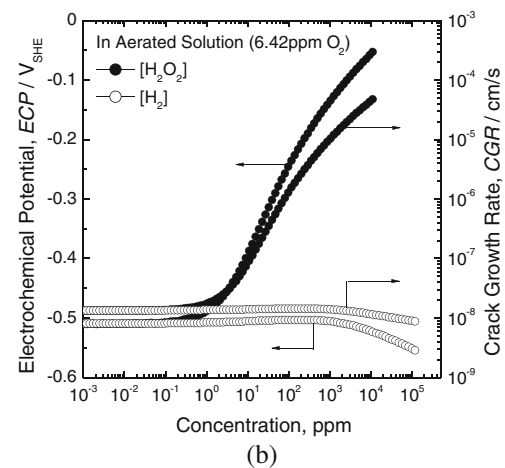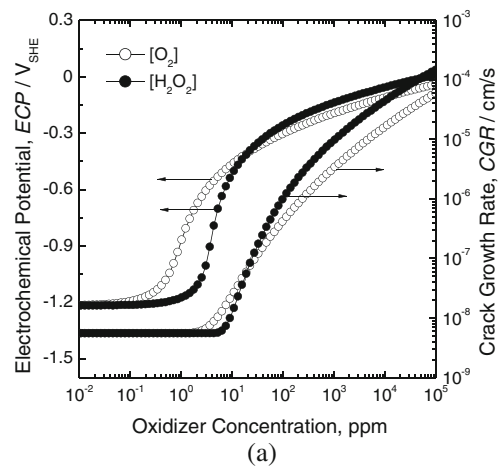

(a)

(b)

Fig. 3 Predicted ECP and CGR vs. **a** oxidizer (O$_2$, H$_2$O$_2$) concentrations for AA5083-H321 in 3.5 wt.% NaCl solution and **b** [H$_2$O$_2$] or [H$_2$] in aerated 3.5 wt.% NaCl solution (6.42 ppm O$_2$ concentration) at pH=7 and at 25 °C. Other parameter values as in Table 2

previous studies [22–25, 30]. Practically, hydrogen water chemistry, which relies upon modification of the redox potential of the environment, has been used as a promising method of mitigating IGSCC of in type 304

Table 2 Default values of parameter in the CEFM for AA5083

Parameter	Value	Comment/source
Concentrations of Na$^+$ and Cl$^-$	1.39×10^4 ppm	3.5 wt.% NaCl solution
Temperature	25 °C	
Crack length (L)	0.5 cm	
Crack opening	0.001 cm	
Crack width	3.81 cm	
Flow velocity	0.001 cm/s	
O$_2$ concentration	1 ppb	
H$_2$ concentration	1 ppb	
H$_2$O$_2$ concentration	1 ppb	

SS in BWR environments and a similar correlation is expected in the case of aluminum alloys. In hydrogen water chemistry, H_2 is added to the feedwater to mitigate IGSCC by depressing the ECP to values below the critical potential, E_{IGSCC}. In addition, using the concentration of H_2O_2 as an independent variable is simply a way of changing the redox conditions of the solution. As noted above, it is likely that these same effects hold in the case of IGSCC in sensitized aluminum alloys in marine environments. Figure 3b depicts dependencies of CGR and ECP on $[H_2]$ and $[H_2O_2]$ for a system containing 6.42 ppm (2.0×10^{-4} m), O_2, i.e., in aerated 3.5 wt.% NaCl solution. At low H_2 or H_2O_2 concentrations, addition of the oxidant or reductant does not give rise to changes in either ECP or CGR. This reflects the fact that the O_2 concentration is so high that O_2 swamps the effects of the other redox species. However, at higher H_2 concentrations, above ~1,000 ppm (0.5 m), an increase in $[H_2]$ induces a shift in the ECP to more negative values, which coincides with the decrease in CGR with increasing H_2 concentration in this range.

Effects of solution conductivity and flow velocity

Figure 4a shows the predicted dependencies of CGR and ECP on solution conductivity for oxygenated environments. The CGR is predicted to be independent of conductivity at low $[O_2]$. Below a certain O_2 concentration [~1 ppm, (3.1×10^{-5} m)], where the ECP is more negative than the critical potential for IGSCC (E_{IGSCC}), the conductivity does not affect the SCC behavior of AA5083-H321 since the CGR is dominated by creep. However, at high O_2 concentration, where the CGR is controlled by environmental effects, the CGR is predicted to be sensitive to conductivity. Increasing the conductivity of the environment (in this case, by changing [NaCl] as the background electrolyte) enhances the throwing power of the current from the crack mouth and gives the external surface a greater capacity to consume electrons being generated by metal dissolution at the crack tip. Thus, the CGR increases. This effect is most marked in high-conductivity environments and is increasingly sensitive to $[O_2]$ above a certain concentration as the conductivity increases. Gao [52] studied the effect of NaCl concentration on the SCC behavior of AA5083-H116 sensitized for 240 h at 175 °C and reported that higher NaCl concentration and lower pH values resulted in shorter incubation time and higher total crack growth. Although the study was conducted with a highly sensitized aluminum alloy, the results indicate that higher solution conductivity leads to higher CGR, in keeping with the theoretical predictions presented here.

From Fig. 4b, it is seen that the CGR is predicted to be independent of $[H_2]$ at low conductivity. In addition, below ~1,000 ppm (0.5 m) of H_2, the CGR is not sensitive to the
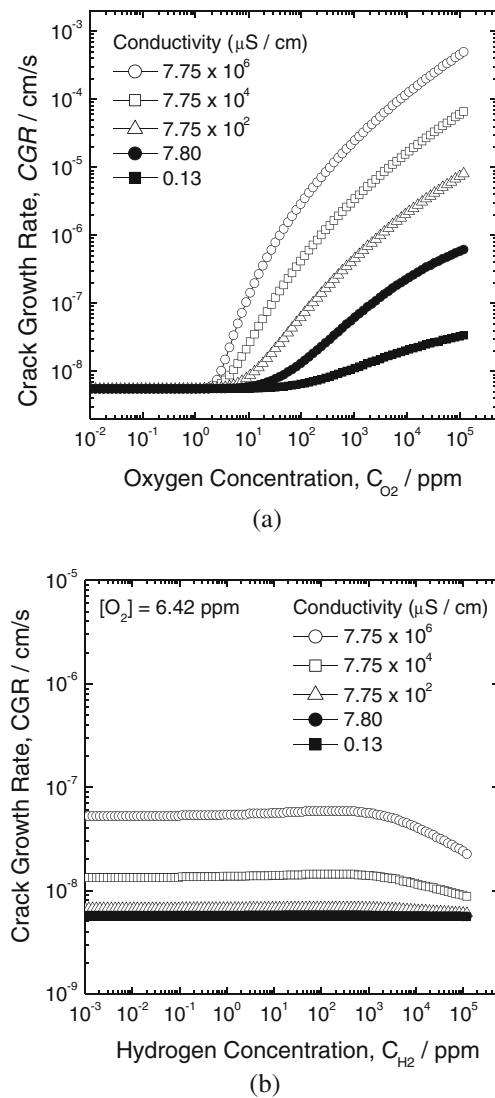

(a)

(b)

Fig. 4 Predicted CGR vs. **a** $[O_2]$ and **b** $[H_2]$ as a function of conductivity for AA5083-H321 in a NaCl solution at pH=7 and at 25 °C. Other parameter values as in Table 2

$[H_2]$ concentration, even in highly conductive solutions, because the O_2 concentration is so high that O_2 masks the effects of hydrogen and the ECP remains almost constant. However, the CGR is predicted to be most dependent upon conductivity at low H_2 concentration and decreases with increasing H_2 concentration above ~1,000 ppm (0.5 m). The decrease in the CGR with increasing H_2 concentration coincides with the predicted shift in ECP to more negative values. However, as is also manifested in Fig. 4, the ECP is not the only factor that determines the CGR. Conductivity, which controls the throwing power of the current from the crack mouth, is predicted to exert a strong influence over the kinetics of crack advance, as shown in Fig. 5. The calculated CGR plotted in Fig. 5 predicts that, at the highest ECP used, the CGR increases by >4 orders of magnitude as the conductivity increases from 0.13 to 7.75×10^6 μS/cm.
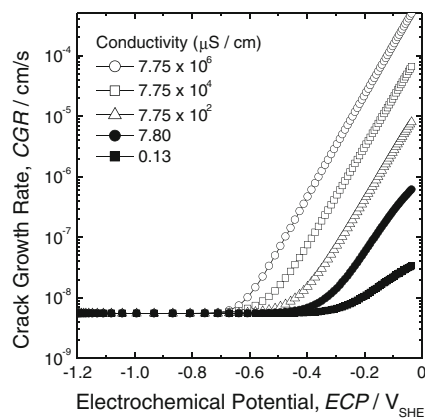
Fig. 5 Predicted CGR vs. ECP as a function of conductivity for AA5083-H321 in a NaCl solution at pH=7 and at 25 °C. Other parameter values as in Table 2

Predicted dependencies of CGR and ECP on flow velocity as a function of [O$_2$] and conductivity are shown in Fig. 6a, b, respectively. In the case of the O$_2$ concentration
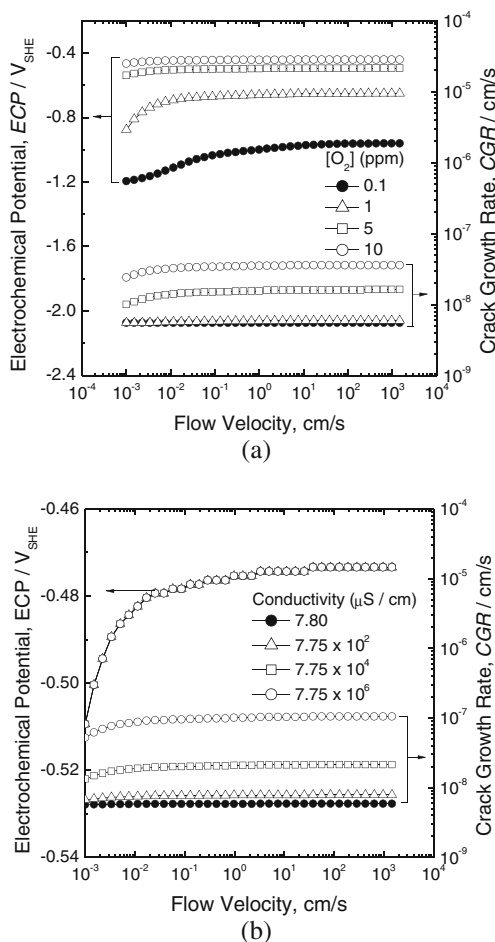

Fig. 6 Predicted ECP and CGR vs. flow velocity **a** with the different [O$_2$] for AA5083-H321 in 3.5 wt.% NaCl solution and **b** at different solution conductivities in a NaCl solution containing 6.42 ppm [O$_2$] at pH=7 and at 25 °C. Other parameter values as in Table 2

effect, the ECP is predicted to be sensitive to flow velocity only at low O$_2$ concentration where mass-transfer effects are most prevalent. However, the CGR is independent of flow velocity at low O$_2$ concentration since the ECP is more negative than E_{IGSCC}. At all values of O$_2$ concentration, at least as being used in these calculations, particularly at high flow velocities, the CGR is predicted to be independent of flow velocity. In these cases, mass transport of O$_2$ to the external surface is not an important factor in controlling the CGR, because the CGR is limited by the throwing power of the current from the crack mouth to the external surface, which is a phenomenon that is sensitive to conductivity. It is important to note that, according to these calculations, IGSCC could be induced in aluminum alloys by increased flow alone (by displacing the ECP above E_{IGSCC}), but, of course, this effect might be somewhat mitigated by a tendency of increased flow to "wash out" the crack and destroy the aggressive conditions (high [Cl$^-$] and high [H$^+$]) that have developed in the crack.

Figure 6b shows the predicted dependencies of CGR and ECP on flow rate as a function of conductivity in an aerated system (6.42 ppm [O$_2$] (2.0×10^{-4} m)). It is noted that the predicted ECP does not depend on conductivity over the conductivity range used in this work. In the CEFM, it is assumed that the exchange current densities and Tafel constants for the redox reactions (H$_2$/H$^+$, O$_2$/H$_2$O, and H$_2$O$_2$/H$_2$O), the kinetic parameters for the alloy dissolution reaction, and the pH, are independent of conductivity, which leads to the independence of the ECP on conductivity. On the other hand, the dependence of CGR on flow velocity is predicted to be a sensitive function of conductivity over the range of very low flow velocity and high conductivity, but the sensitivity is less significant as compared with those of [O$_2$] and conductivity. In the aerated solution having highest conductivity (7.75 S/cm in this calculation), the CGR is predicted to only increase from 5.21×10^{-8} to 1.05×10^{-7} cm/s as the flow velocity increases from 0.001 to 1,000 cm/s, indicating a low sensitivity of the CGR to mass transport effects.

Effect of stress intensity factor

In the CEFM, increasing stress intensity factor, K_I, increases the frequency of rupture of the passive film at the crack tip and enhances the CGR. However, at higher O$_2$ concentrations such as those that exist in an aerated marine environment, the CGR is not only greater than the creep rate but is only weakly dependent on K_I, particularly in solutions of conductivity of 0.0775 S/cm, as shown in Fig. 7. In lower conductivity solutions, the CGR is more dependent on K_I, due to insufficient throwing power of the current from the
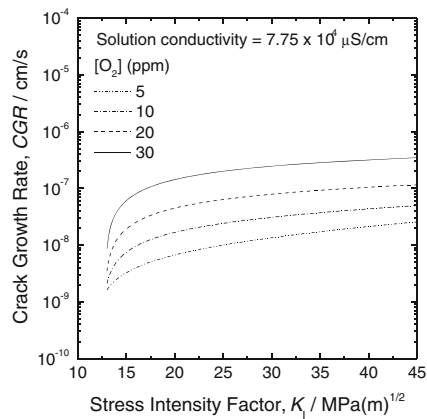
Fig. 7 Predicted CGR vs. K_I for AA5083-H321 in 3.5 wt.% NaCl solution containing different $[O_2]$ at pH=7 and at 25 °C. Other parameter values as in Table 2

crack mouth across the external surface. The dependence of the CGR on K_I is particularly important, since it defines the lower limit to the rate of crack advance. For a value of K_I=25 MPa√m, the CGR of AA5083-H321 at 25 °C is estimated to be ~5.5×10^{-9} cm/s, which is in good agreement with the CGR for ECP values more negative than approx. −0.6 V_{SHE}. Crack advance is not predicted below some threshold stress intensity level (corresponding to K_{ISCC}) in a typical SCC experiment. In any event, for the conditions employed in calculating the CGR shown in Fig. 7, the value of K_{ISCC} is estimated to be about ~13.0 MPa√m, although the exact value does appear to depend upon the conditions assumed, as expected. The value of K_{ISCC} in the present work is in good agreement with the experimental value of Al–Mg alloy [53, 54]. Holtz et al. [53] measured the K_{ISCC}, in 1% NaCl solution containing inhibitor, of the as-received and fully sensitized (240 h at 175 °C) AA5083-H131 using rising stress step loading tests. The K_{ISCC} values were estimated to be about 20 and 3 MPa√m, for the as-received and fully sensitized AA5083-H131, respectively. Crane and Gangloff [54] reported the correlation between the DoS and the K_{ISCC} of AA5083-H131 sensitized at 100 °C. For intermediate levels of sensitization, between the fully sensitized and unsensitized conditions, K_{ISCC} changed linearly with the DoS and the K_{ISCC} of AA5083-H131 having the DoS value of 10 mg/cm^2 was in the range of 13–15 MPa√m. Recently, Lim et al. [55] studied intergranular corrosion (IGC) penetration in an Al–Mg alloy as a function of electrochemical and metallurgical conditions. IGC penetration rate might be equated to the CGR for K_I slightly greater than K_{ISCC} (to allow for corrosion product wedging). They measured IGC penetration depth into AA5083-H131 specimens sensitized at 100 and 80 °C in 0.6 M NaCl solution at pH=8.3 and at −0.49 V_{SHE}. It was recognized that IGC penetration rate

depended on applied potential, DoS, exposure time, and propagation direction and the specimens having the same DoS, but sensitized at different temperatures, showed very different IGC propagation rates. IGC penetration rates in a longitudinal direction for AA5083-H131 having DoS values of 2 and 10 mg/cm^2 were 1.3 (±0.9)×10^{-8} and 2.5 (±0.9)× 10^{-8} cm/s, respectively. These penetration rates are an order of magnitude higher than the calculated CGR (2.0× 10^{-9} cm/s at 13.2 MPa√m at OCP) for K_I being slightly greater than K_{ISCC}. However, when we consider that the initial crack length used in this work is greater and that the applied potential was a little more positive than the OCP, both of which impact the CGR (the CGR decreases with increasing crack length), the calculated CGR for K_I being slightly greater than K_{ISCC} is in reasonable agreement with experiment.

Above a threshold stress intensity, the CGR of aluminum alloys increases rapidly with increasing K_I and then reaches a plateau velocity that is practically independent of K_I. This plateau velocity is characteristic of the alloy/environment combination and is the result of electrochemical processes limiting the rate of crack propagation, as embodied in the CEFM. This type of behavior is displayed by many alloy/environment combinations, including IGSCC in sensitized type 304 SS in high-temperature water, for example [31]. In that case, the frequency of the microfracture events occurring at the crack front varies with K_I in like fashion, demonstrating that a change in CGR, for whatever reason, occurs because of a change in event frequency, with the microfracture event dimension being more-or-less constant and probably determined by precipitate spacing on the grain boundary or by the diffusion length of hydrogen ahead of the crack tip.

There are several studies supporting HIC as a key factor in the mechanism of crack advance in the SCC of an Al–Mg alloy having a low DoS [3, 11–13, 16]. For instance, Jones [12] reported considerable evidences that hydrogen is produced at the crack tip of AA5083 that contain β-phase precipitates along grain boundaries and hydrogen uptake occurs during corrosion of aluminum alloys including AA5083 as shown by resistivity change and thermal desorption. As shown in our work on type 304 SS in high-temperature water [31], fracture mechanics controls the microfracture frequency, but hydrogen embrittlement determines the microfracture size. As noted above, if the SDR model was correct, the microfracture dimension should be a few Burger's vectors or a few nanometers in magnitude, but experimentally it is found to be 2–3 μm. Thus, if the SDR model was viable, the event frequency would have to be in the kilohertz range rather than 0–2 Hz observed experimentally by analysis of the coupling current. For sensitized type 304 SS in thiosulfate containing solutions [34, 35] and for AISI 4340 high-strength steel in caustic environments [36],

both of which are well-known HIC systems, the microfracture dimension can exceed the grain size and it is this large microfracture dimension that results in the high CGR.

Figure 8a, b shows the predicted microfracture event frequency and dimension for AA5083-H321 in 3.5 wt.% NaCl solution as a function of K_I and CGR, respectively. At low K_I (below 18 MPa√m), the microfracture event frequency is predicted to increase dramatically from 8.4×10^{-8} to 1.6×10^{-4} Hz and the predicted microfracture dimension decreases from 1980 to 92.6 μm, but above 18 MPa√m, the increase of the frequency and the decrease of the dimension are less significant (~1 order in magnitude increase in the frequency and the microfracture dimension decreases from 92.6 to 42.5 μm as K_I changes from 18 to 45 MPa√m). The dependence of the microfacture frequency on K_I (Fig. 8a) parallels closely the dependence of CGR on K_I

(Fig. 7), implying that the CGR is controlled by the microfracture frequency, not by changes in the microfracture dimension, a finding that was also made experimentally for IGSCC in sensitized type 304 SS in high-temperature water [31]. This is also shown by the linear dependence of CGR on microfracture event frequency in Fig. 8b, in which microfracture event frequency is predicted to increase linearly with CGR from 1.0×10^{-8} to 6.6×10^{-5} cm/s as the microfracture frequency increases from 4.5×10^{-4} to 6.5 Hz. The predicted microfracture dimension changed from 65 to 44 μm over the selected CGR range (Fig. 8b). For AA5083-H321 in 3.5 wt.% NaCl solution at the OCP and at K_I=25 MPa√m, the microfracture event frequency and microfracture dimension are 0.00076 Hz and 57.8 μm, respectively, which strongly suggests that HIC is the basic mechanism of microfracture. This is so, because in the classical SDR mechanism, the microfracture dimension should be a small multiple of the Burgers vector for the slip system or nm in dimension, as postulated elsewhere for IGSCC in sensitized type 304 SS in thiosulfate solution [34, 35] and in AISI4340 high-strength steel in caustic solutions [36]. The predicted microfracture frequency is 1–2 orders of magnitude lower than those found experimentally for sensitized type 304 SS in thiosulfate solution (0.1–0.01 Hz) and for sensitized AISI4340 high-strength steel in caustic solutions (0.003 Hz), but the microfracture dimension is comparable (>100 μm for type 304 SS, 49 μm for AISI4340 high-strength steel, and 57.8 μm for AA5083-H321). The complete resolution of this issue requires the measurement of the coupling current and the noise contained therein as a function of K_I and other properties [31, 34–36]. These studies are underway and will be reported in a subsequent paper.

Predicted effects of the multiplier of the standard exchange current density and crack length

Modeling studies with the CEFM for type 304 SS in BWR environment have revealed the effects of noble metal and inhibitory dielectric coatings on the predicted CGR [23]. From an electrochemical viewpoint, noble metal coatings are expected to increase the standard exchange current densities (SECD) of the redox reactions (H_2 oxidation and O_2 and H_2O_2 reduction), while inhibitory dielectric coatings could be expected to decrease the SECDs. It is likely that these effects also hold in the case of IGSCC in sensitized aluminum alloys, as they do for fracture in stainless steel. Catalysis implies the factor that is used to multiply the SECD is >1. Inhibition implies a multiplication factor of <1. Calculations reported here are limited in scope, particularly with regard to composition of the environment. Figure 9 shows results of the calculations for oxygenated environments, in which the conductivity and K_I are held
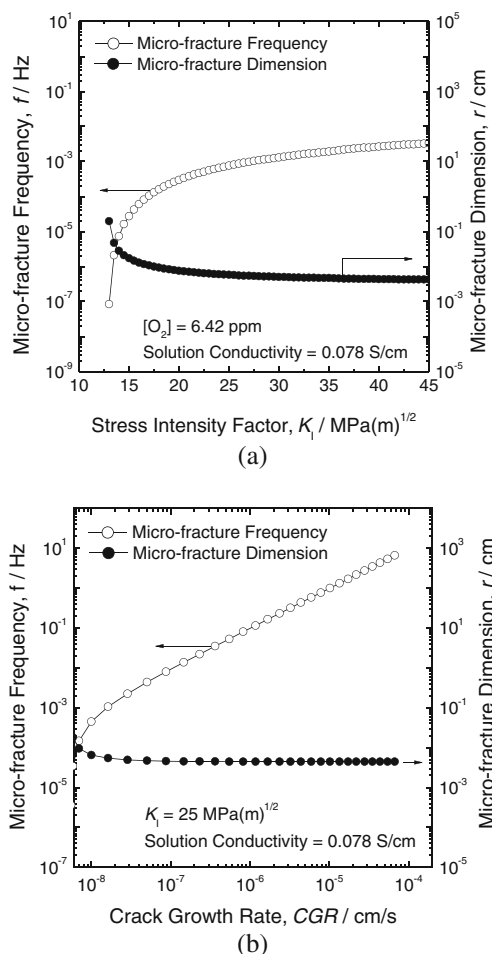
Fig. 8 Calculated microfracture event frequency and microfracture dimension as functions of **a** K_I (for $[O_2]$=6.42 ppm) and **b** CGR (for K_I=25 MPa√m) based on the treatment of Shoji et al. for crack tip strain rate for AA5083-H321 in 3.5 wt.% NaCl solution at 25 °C. Other parameter values as in Table 2
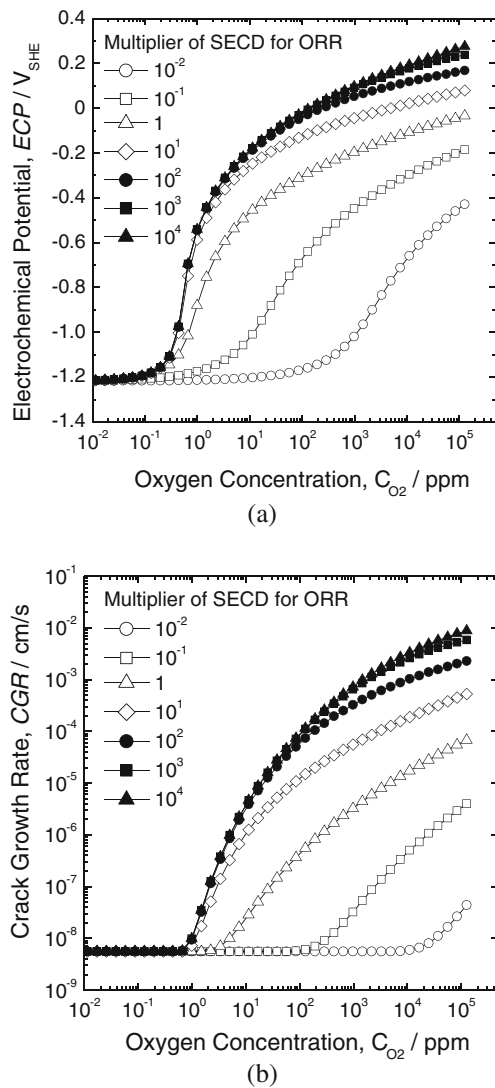
Fig. 9 Predicted **a** ECP and **b** CGR vs. [O$_2$] for AA5083-H321 under specific catalysis conditions and the multiplier of the SECD for ORR (oxygen reduction reaction) in 3.5 wt.% NaCl solution at pH=7 and at 25 °C. Other parameter values as in Table 2

reduction is equivalent to lowering the concentration under conditions where the SECD is maintained constant. Thus, specific inhibition is predicted to be effective in reducing the CGR.

As reported in our previous work for type 304 SS in BWR environments [23], it was expected that the CGR would be strongly dependent on crack length under constant K_I conditions, due to the strong coupling between the internal and external crack environments and the IR potential drop down the crack. Figure 10 depicts this dependence and shows the predicted CGR as a function of ECP, as the crack length is varied from 0.001 to 10 cm. For these calculations, K_I=25 MPa√m and the treatment of Shoji et al. [56] for estimating the crack-tip strain rate was used. The calculated CGR plotted in Fig. 10 predict that, at the highest ECP used, the CGR decreases by ~2 orders of magnitude as the crack length increases from 0.001 to 10 cm. The longer crack therefore produces a lower CGR. The decrease in CGR, as the crack length increases, is directly attributable to the IR potential drop, as has been argued previously in papers [23, 25] on the CEFM. Thus, the longer the crack, the higher is the IR potential drop down the crack, the less is the potential drop across the external surface that drives O$_2$ reduction, and hence the lower is the CGR. It is also recognized that the E_{IGSCC}, the minimum ECP at which the environmentally induced CGR becomes distinguishable from crack extension resulting from creep, becomes more positive as the crack length increases, indicating a theoretical dependence of the E_{IGSCC} on crack length. The shortest crack length resulted in the most negative E_{IGSCC}.

The dependence of the CGR on crack length provides a ready explanation for the shapes of cracks in plane surfaces (i.e., "surface cracks"). The CEFM predicts that, as the

constant at 0.0775 S/cm and 25.0 MPa√m, respectively, and the SECD multiplier for O$_2$ reduction is changed from 10^4 (strong catalysis) to 10^{-2} (strong inhibition). The modeling predicts that CGR and ECP are strong functions of SECD for O$_2$ reduction reaction. However, catalysis and inhibition of the O$_2$ reduction reaction do not affect the CGR at low [O$_2$], where the CGR is controlled by creep. In addition, for higher values of multiplier (more than ~100) the CGR and the ECP are predicted to be independent of the catalysis conditions. When the SECD for O$_2$ reduction reaction is sufficiently high, overall kinetic and ECP are restricted by the mass transfer of O$_2$ to the external surface. Finally, the CGR reflects the changes in the ECP, recognizing that lowering the SECD for O$_2$
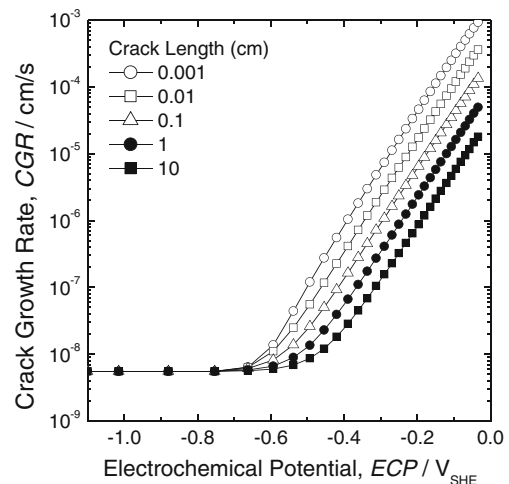

Fig. 10 Predicted CGR vs. ECP as a function of initial crack length for AA5083-H321 in 3.5 wt.% NaCl solution, at pH=7 and at 25 °C. Other parameter values as in Table 2

initial crack length increases, the CGR decreases and that the crack propagation rates along the surface and perpendicular to the surface are different. If L_{major} and L_{minor} represent the crack length along and perpendicular to the surface, respectively, they can be expressed by the following recursive equations.

$$L_{minor}(j+1) = L_{minor}(j) + \left(\frac{dL}{dt}\right)_{L=L(j)} \times \Delta t$$
$$L_{major}(j+1) = L_{major}(j) + \left(\frac{dL}{dt}\right)_{L=L^o} \times \Delta t$$

where L^o is initial crack length, Δt is time increment, and $\left(\frac{dL}{dt}\right)_{L=L(j)}$ represents a CGR at $L=L(j)$, which is the shortest distance between the crack front and the external surface at this location. For growth at the edge, along the surface, the value of crack length for the next time increment has a linear relationship with time because the CGR at the edge is a constant at L^o.

Figure 11a shows the predicted CGR with respect to time for AA5083-H321 in aerated 3.5 wt.% NaCl solution at pH=7 and at 25 °C. The CGR along the minor axis of the semi-ellipse (normal to the surface) decreases, resulting in an overall shorter crack length along the minor axis than in the case of the major axis along the surface. Thus, the crack grows along the surface with a constant CGR that is higher than that at the center of crack, resulting in the progressive development of a longer crack length on the major axis of the semi-ellipse than on the minor axis. While the crack lengths on the major and minor axes are initially equal, a discrepancy quickly develops between the rates of crack propagation along the two different axes over specific time interval. This behavior leads to the progressive development of a semi-elliptical surface cracks that are frequently observed in SCC, as shown in Fig. 11b.

Summary and conclusions

In order to assess the importance of IGSCC in aluminum alloys, we have modified and calibrated the CEFM, which has been used extensively to predict IGSCC in sensitized austenitic stainless steel components in the heat transport circuits of nuclear power reactors, to predict CGRs in marine aluminum alloys. Calibration involves optimization of the CEFM on measured CGR data and, after extracting values for essential parameters, calculating CGR data as a function of the independent variables of interest. The customized CEFM for aluminum alloys provided quantitative predictions of the effects of O_2, electrochemical potential, stress intensity factor, and conductivity on CGR in lightly sensitized AA5083-H321 in 3.5 wt.% NaCl solution. The importance of environmental variables, such as conductivity
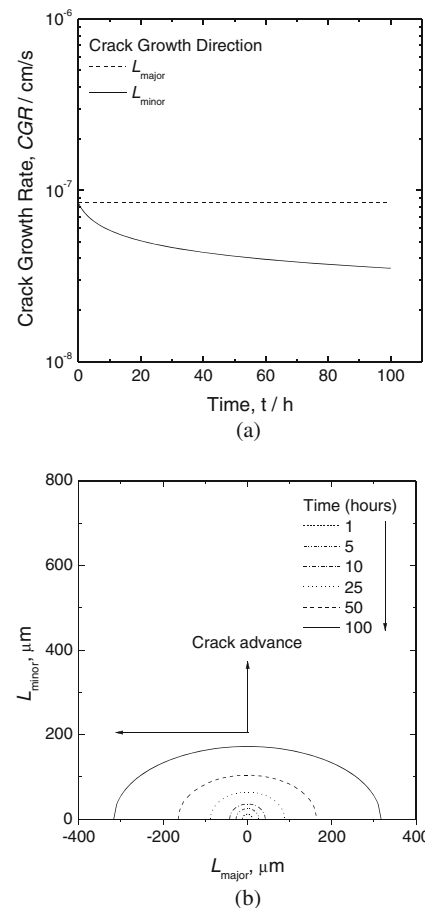

(a)

(b)

Fig. 11 Predicted **a** CGR with respect to elapsed time and **b** evolution of shape for a surface crack in a plane surface of AA5083-H321 in aerated 3.5 wt.% NaCl solution (6.42 ppm O_2 concentration) at pH=7 and at 25 °C. Other parameter values as in Table 2. L_{major} and L_{minor} represent the crack length along and perpendicular to the surface, respectively

and oxidant/reductant concentration, on the IGSCC of lightly sensitized AA5083-H321 in a marine environment has also been confirmed. In addition, the CEFM provides a mechanistic definitions of E_{IGSCC} and K_{ISCC} in lightly sensitized AA5083-H321 in 3.5 wt.% NaCl solution. Furthermore, the CEFM provides a ready explanation for the shapes of cracks in plane surfaces; that is, the progressive development of a semi-elliptical surface cracks. The success of the CEFM in accounting for the IGSCC of Al–Mg alloys, argues that the basic concept of the model, in which the internal and external environments are strongly coupled by the conservation of charge, is sound and is as applicable to IGSCC in lightly sensitized aluminum alloys as it is for other alloys.

References

1. Searles JL, Gouma PI, Buchheit RG (2001) Stress corrosion cracking of sensitized AA5083 (Al–4.5Mg–1.0Mn). Metall Mater Trans A 32:2859–2867

2. Vassilaros MG (1994) In: Parkins RN (ed) Life prediction of corrodible structures. NACE International, Houston, pp 1656–1667

3. Jones RH, Baer DR, Danielson MJ, Vetrano JS (2001) Role of Mg in the stress corrosion cracking of an Al–Mg alloy. Metall Mater Trans A 32:1699–1711

4. Pickens JR, Gordon JR, Green JAS (1983) The effect of loading mode on the stress-corrosion cracking of aluminum alloy 5083. Metal Trans A 14A:925–930

5. Lea C, Molinari C (1984) Magnesium diffusion, surface segregation and oxidation in Al–Mg alloys. J Mater Sci 19:2336–2352

6. Vetrano JS, Williford RE, Buremmer SM, Jones RH (1997) Influence of microstructure and thermal history on the corrosion susceptibility of AA5083. In: Das SK (ed) Automotive alloys, vol. 77. TMS Annual Meeting, Orlando, FL, p 77

7. Sampath D, Moldenhauer S, Schipper HR, Mechsner K, Haszler A (2000) Decomposition of solid solution of the AA5083 alloy upon exposure to elevated temperatures. Mater Sci Forum 331–337:1089–1094

8. Windisch CFJ, Baer DR, Engelhard MH, Danielson MJ, Jones RH (2000) Corrosion of Mg- and Cu-implanted Al in 3.5 % NaCl solution. In: 198th Meeting of the Electrochemical Society

9. Baer DR, Windisch CF, Engelhard MH, Danielson MJ, Jones RH, Vetrano JS (2000) Influence of Mg on the corrosion of Al. J Vac Sci Technol A 18:131–136

10. Searles JL, Gouma PI, Buchheit RG (2002) Stress corrosion cracking of sensitized AA5083 (Al–4.5Mg–1.0Mn). Mater Sci Forum 396–402:1437–1442

11. Tanguy D, Bayle B, Dif R, Magnin T (2002) Hydrogen effects during IGSCC of pure Al–5Mg alloy in NaCl media. Corros Sci 44:1163–1175

12. Jones RH (2003) The influence of hydrogen on the stress-corrosion cracking of low-strength Al–Mg alloys. JOM 55:42–46

13. Jones RH, Vetrano JS, Windisch CF (2004) Stress corrosion cracking of Al–Mg and Mg–Al alloys. Corrosion 60:1144–1154

14. Davenport AJ, Yuan Y, Ambat R, Connolly BJ, Strangwood M, Afseth A, Scamans GM (2006) Intergranular corrosion and stress corrosion cracking of sensitised AA5182. Mater Sci Forum 519–521:641–646

15. Oguocha IN, Adigun OJ, Yannacopoulos S (2008) Effect of sensitization heat treatment on properties of Al–Mg alloy AA5083-H116. J Mater Sci 43:4208–4214

16. Gao J, Quesnel D (2011) Enhancement of the stress corrosion sensitivity of AA5083 by heat treatment. Metall Mater Trans A 42:356–364

17. Doig P, Jones GT (1977) A model for the initiation of hydrogen embrittlement cracking at notches in gaseous hydrogen environments. Metall Trans A 8:1993–1998

18. Ford FP, Silverman MJ (1980) The prediction of stress-corrosion cracking of sensitized 304 stainless-steel in 0.01M Na$_2$SO$_4$ At 97 °C. Corrosion 36:558–565

19. Ford FP, Andresen PL (1987) The theoretical prediction of the effect of system variables on the cracking of stainless steel and its use in design. Corrosion/87, San Francisco, CA

20. Ford F, Taylor D, Andresen P, Ballinger R (1987) Corrosion-assisted cracking of stainless and low-alloy steels in LWR environments. EPRI Report (Project 2006-6)

21. Li R, Ferreira MGS (1996) The thermodynamic conditions for hydrogen generation inside a stress corrosion crack. Corros Sci 38:317–327

22. Macdonald DD, Urquidi-Macdonald M (1991) A coupled environment model for stress corrosion cracking in sensitized type 304 stainless steel in LWR environments. Corros Sci 32:51–81

23. Macdonald DD, Lu P-C, Urquidi-Macdonald M, Yeh T-K (1996) Theoretical estimation of crack growth rates in type 304 stainless steel in boiling-water reactor coolant environments. Corrosion 52:768–785

24. Macdonald DD (1996) On the modeling of stress corrosion cracking in iron and nickel base alloys in high temperature aqueous environments. Corros Sci 38:1003–1010

25. Engelhardt G, Urquidi-Macdonald M, Macdonald DD (1997) A simplified method for estimating corrosion cavity growth rates. Corros Sci 39:419–441

26. Turnbull A (1997) Modelling of crack chemistry in sensitized stainless steel in boiling water reactor environments. Corros Sci 39:789–805

27. Boellinghaus T, Hoffmeister H (2000) Numerical model for hydrogen-assisted cracking. Corrosion 56:611–622

28. Chateau JP, Delafosse D, Magnin T (2002) Numerical simulations of hydrogen–dislocation interactions in FCC stainless steels: part I: hydrogen–dislocation interactions in bulk crystals. Acta Mater 50:1507–1522

29. Chateau JP, Delafosse D, Magnin T (2002) Numerical simulations of hydrogen–dislocation interactions in FCC stainless steels.: part II: hydrogen effects on crack tip plasticity at a stress corrosion crack. Acta Mater 50:1523–1538

30. Vankeerberghen M, Macdonald DD (2002) Predicting crack growth rate vs. temperature behaviour of type 304 stainless steel in dilute sulphuric acid solutions. Corros Sci 44:1425–1441

31. Manahan MP, Macdonald DD, Peterson AJ (1995) Determination of the fate of the current in the stress corrosion cracking of sensitized type 304SS in high temperature aqueous systems. Corros Sci 37:189–208

32. Macdonald DD, Scott AC, Wentrcek P (1981) Redox potential measurements in high temperature aqueous systems. J Electrochem Soc 128:250–257

33. Scully JC (1980) The interaction of strain-rate and repassivation rate in stress corrosion crack propagation. Corros Sci 20:997–1016

34. Gomez-Duran M, Macdonald DD (2003) Stress corrosion cracking of sensitized type 304 stainless steel in thiosulfate solution: I. Fate of the coupling current. Corros Sci 45:1455–1471

35. Gomez-duran M, Macdonald DD (2006) Stress corrosion cracking of sensitized type 304 stainless steel in thiosulphate solution. II. Dynamics of fracture. Corros Sci 48:1608–1622

36. Liu S, Macdonald DD (2002) Fracture of AISI 4340 steel in concentrated sodium hydroxide solution. Corrosion 58:835–845

37. Vijh AK (1968) Electrolytic hydrogen evolution reaction on aluminum in acidic solutions. J Phys Chem 72:1148–1156

38. Grosskreutz JC (1969) Mechanical properties of metal oxide films. J Electrochem Soc 116:1232–1237

39. Frost HJ, Ashby F (1982) Deformation-mechanism maps: the plasticity and creep of metals and ceramics. Pergamon, Oxford. pp. 20–29

40. Moon S, Pyun S (1998) Faradaic reactions and their effects on dissolution of the natural oxide film on pure aluminum during cathodic polarization in aqueous solutions. Corrosion 54:546–552

41. Chang JC, Chuang TH (2000) The degradation of corrosion resistance for Al 5083 alloy after thermal and superplastic forming processes. J Mater Eng Perform 9:253–260

42. Bard AJ, Faulkner LR (2000) Electrochemical methods: fundamentals and applications, 2nd edn. Wiley, New York

43. Hsiao IC, Huang JC (2002) Deformation mechanisms during low- and high-temperature superplasticity in 5083 Al–Mg alloy. Metall Mater Trans A 33:1373–1384

44. Liu Y, Cheng YF (2009) Cathodic reaction kinetics and its implication on flow-assisted corrosion of aluminum alloy in aqueous ethylene glycol solution. J Appl Electrochem 39:1267–1272
45. ASM Material Data Sheet. http://asm.matweb.com/search/SpecificMaterial.asp?bassnum=MA5083H116
46. ASTM G-67 (2004) Standard test method for determining the susceptibility to intergranular corrosion of 5xxx series aluminum alloys by mass loss after exposure to nitric acid (NAMLT test). Annual Book of ASTM Standards
47. Garcia HE, Gordon LI (1992) Oxygen solubility in seawater: better fitting equations. Limnol Oceanogr 37:1307–1312
48. Wilkinson DS, Vitek V (1982) The propagation of cracks by cavitation: a general theory. Acta Metall 30:1723–1732
49. Lu C, McDonald KT (1997) The effect of annealing on creep of aluminum wire. Princeton University, Princeton. pp. 1–14
50. Bencivenni G, Bucci L, Finocchiaro G, Forti C (1998) Creep measurement on aluminum-5056 wires. KLOE, Frascati, Italy. pp. 1–13
51. Kaufman JG (1999) Properties of aluminum alloys: tensile creep and fatigue data at high and low temperatures. ASM International, Materials Park, OH
52. Gao J (2011) Experiments to explore the mechanisms of stress corrosion cracking. Ph.D. thsis, University of Rochester
53. Holtz RL, Pao PS, Bayles RA, Longazel TM, Goswami R (2011) Corrosion-fatigue behavior of aluminum alloy 5083-H131 sensitized at 448 K (175 °C). Metall Mater Trans A 43:2839–2849
54. Crane CB, Gangloff RP (2011) Stress corrosion cracking of low temperature sensitized AA5083. In: Department of Defense 2011 Corrosion Conference. NACE, Houston. pp. 1–14
55. Lim MLC, Scully JR, Kelly RG (2013) Intergranular corrosion penetration in an Al–Mg alloy as a function of electrochemical and metallurgical conditions. Corrosion 69:35–47
56. Shoji T, Lu Z, Murakami H (2010) Formulating stress corrosion cracking growth rates by combination of crack tip mechanics and crack tip oxidation kinetics. Corros Sci 52:769–779